https://doi.org/10.5194/essd-2024-169
Preprint. Discussion started: 5 August 2024

A high-resolution pan-Arctic meltwater discharge dataset from 1950 to 2021

Adam Igneczi[1*], Jonathan Bamber[1,2]

[1]Bristol Glaciology Centre, School of Geographical Sciences, University of Bristol, UK

[2]Department of Aerospace and Geodesy, Technical University of Munich, Germany

* *Correspondance: Ádám Ignéczi <a.igneczi@bristol.ac.uk, ignecziadam@gmail.com>*

Abstract

Arctic air temperatures have increased about four times faster than the global average since about 1980. Consequently the Greenland Ice Sheet has lost about twice as much ice as the Antarctic Ice Sheet between 2003 and 2019, and mass loss from glaciers and ice caps is also dominated by those that lie in the Arctic. Thus, Arctic land ice loss is currently a major contributor to global sea level rise. This increasing freshwater flux into the Arctic and North Atlantic oceans, will also impact physical, chemical and biological processes across a range of domains and spatiotemporal scales. Although, meltwater discharge data at Arctic coastlines are available from two existing datasets, these are limited by their spatial resolution and/or coverage. Here, we improve upon previous work and provide a high-resolution coastal meltwater discharge data product that covers all Arctic regions, where land ice is present, i.e. the Canadian Arctic Archipelago, Greenland, Iceland, Svalbard, Russian Arctic Islands. Coastal meltwater discharge data were derived from Modèle Atmosphérique Régional daily ice and land runoff products between 1950 and 2021, which we statistically downscaled from their original ~6 km resolution to 250 m. The complete data processing algorithm, including downscaling, is fully documented and relies on open-source software. The coastal discharge database is disseminated in easily accessible and storage efficient netCDF files.

https://doi.org/10.5194/essd-2024-169
Preprint. Discussion started: 5 August 2024

1. Introduction

Arctic air temperatures have warmed about four times faster than the global average during the last four decades (Rantanen et al., 2022). One of the consequences of this is increasing land ice loss. The Greenland Ice Sheet (GrIS) has lost about twice as much mass as the Antarctic Ice Sheet between 2003 and 2019 (Smith et al., 2020, IPCC, 2021). Over the same period, glaciers and ice caps (GIC) in the Arctic – i.e. in Alaska, Canadian Arctic Archipelago, Iceland, Svalbard, Russian Arctic Islands – and peripheral GIC (PGIC) in Greenland were responsible for about 71% of the global GIC mass loss (Hugonnet et al., 2021). Altogether the GrIS and Arctic GIC lost a similar amount of ice during the last two decades. The rate of land ice loss has also been reported to have accelerated across the Arctic, except for Iceland (Ciracì et al., 2020), over the last few decades. Notably, mass loss rate in Greenland – i.e. the ice sheet and its PGICs – has been estimated to have increased sixfold between 1980 and 2020 (Mouginot et al., 2019). Due to these processes, Arctic land ice loss is currently a major contributor to global sea level rise (Frederikse et al., 2020; IPCC, 2021) and to the freshwater budget of the Arctic and North Atlantic oceans (Bamber et al, 2018).

Arctic GIC and the GrIS lose mass through a combination of decreasing surface mass balance – i.e. increasing surface runoff relative to precipitation – and increasing solid ice discharge (hereafter termed discharge). Although about two-thirds of the net mass loss from the GrIS between 1972-2018 is attributable to discharge (Mouginot et al., 2019), the relative contribution of this process has diminished to about 30-50% since 2000 due to increasing surface runoff (Enderlin et al., 2014; van den Broeke et al., 2016; Mouginot et al., 2019; King et al., 2020). This process plays an even more prominent role in land ice loss elsewhere in the Arctic; about 87% of the GIC mass loss between 2000 and 2017 across the Canadian Arctic Archipelago, Iceland, Svalbard, and the Russian Arctic Islands has been attributed to decreasing surface mass balance (Tepes et al., 2021). These trends illustrate the growing role of liquid meltwater discharge into Arctic seas, impacting physical, chemical and biological processes across a range of domains and spatiotemporal scales (Catania et al., 2020). Meltwater discharge at the ice-ocean interface of tidewater glaciers can also modulate discharge by influencing calving rates and ice dynamics (e.g.: Cowton et al., 2019; Melton et al., 2022). However, perhaps most importantly, increasing glacial freshwater flux – consisting of meltwater discharge and solid ice discharge – can influence the large-scale oceanic

https://doi.org/10.5194/essd-2024-169
Preprint. Discussion started: 5 August 2024

circulation of the Arctic and sub-Arctic North Atlantic (SNA) Oceans (e.g.: Boning et al., 2016; Gillard et al., 2016; Yang et al., 2016; Dukhovskoy et al., 2019; Biastoch et al., 2021) and potentially the Arctic climate (Proshutinsky et al., 2015).

Despite its importance for a wide range of processes at varying spatiotemporal scales, only two studies provide data covering a multi-decadal time span over most, but not all, of Arctic land ice. These datasets rely on Regional Climate Model (RCM) runoff products – Modèle Atmosphérique Régional (MAR) and/or Regional Atmospheric Climate Model (RACMO) – digital elevation models, ice masks, statistical downscaling and meltwater routing algorithms to estimate coastal surface runoff fluxes. Bamber et al. (2018) utilise RACMO products (1958-2016) and cover most of the Arctic and Sub-polar North Atlantic (SNA) Oceans region with significant land ice presence, except for the Russian Arctic Islands. Although the coverage is fairly comprehensive, the data have a relatively low spatial (5 km) and temporal (monthly) resolution. Mankoff et al., (2020) use both RACMO and MAR products (1950-2021) to provide high resolution data – daily, 100 m; with modelled runoff inputs downscaled from 7.5 km (MAR) and 5.5 km (RACMO) to 1 km – but only for Greenland. Here, we combine the advantages of these two datasets and provide a high resolution (daily, 250m) meltwater discharge dataset for the period of 1950-2022 in an easily accessible and storage efficient database that covers the most important land ice sectors of the Arctic and SNA Oceans region, i.e. Canadian Arctic Archipelago, Greenland, Iceland, Svalbard, Russian Arctic Islands.

https://doi.org/10.5194/essd-2024-169
Preprint. Discussion started: 5 August 2024

2. An overview of the data processing pipeline

Our goal is to obtain a high resolution coastal meltwater discharge product that partitions meltwater according to its source, i.e. tundra, ice surface, and ice surface below the snowline (i.e. bare ice). To achieve this, we first downscaled coarse resolution (~ 6 km) RCM products (ice and tundra runoff, ice albedo; the latter to approximate the bare ice coverage) using their native vertical gradients and high resolution (90 m) surface DEMs (Figure 1). Limitations due to coarse resolution ice and land masks supplied with the RCM were addressed during this step by integrating high-resolution (250 m) ice and land masks into the downscaling algorithm (Figure 1). The high-resolution surface DEM that is used in the downscaling process is also used to delineate drainage basins and coastal outflow points in a hydrological routing algorithm. These drainage basins are used to sum the daily meltwater runoff and estimate meltwater discharge at the corresponding coastal outflow points (Figure 1). In order to limit computational requirements needed at any one time, we carried out the above process separately for each major glacier region. These are delineated according to the first order regions defined in in the Randolph Glacier Inventory v.6.0 (RGI Consortium, 2017): RGI-03 (Arctic Canada North), RGI-04 (Arctic Canada South), RGI-05 (Greenland), RGI-06 (Iceland), RGI-07 (Svalbard and Jan Mayen), RGI-09 (Russian Arctic

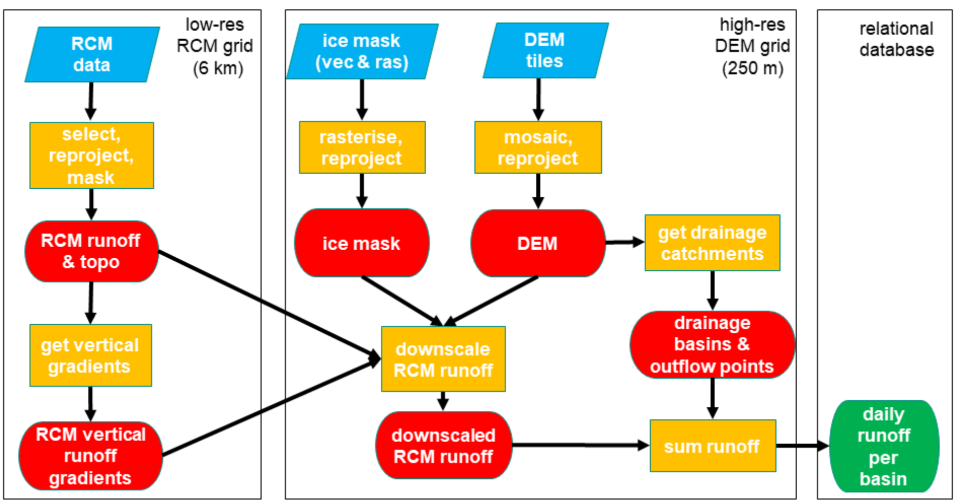

Figure 1. Data pipeline

https://doi.org/10.5194/essd-2024-169
Preprint. Discussion started: 5 August 2024

Open Access Earth System Science Data Discussions

3. Input data pre-processing

3.1. Static data

We assumed that time dependent changes in surface topography, land and ice extent have negligible impact on large-scale surface runoff during our period of interest, i.e. between 1950-2022. Hence we used static data products to obtain information about these physical properties.

3.1.1. DEM and land-ocean mask

High resolution (3"; ~90 m) DEMs were obtained from the Copernicus GLO-90 DGED DEM product (ESA, 2021). This DEM is distributed in 1°x1° tiles and is referenced on the WGS-84 ellipsoid. This product is in several ways superior to ArcticDEM – unless very high resolution (i.e. up to 1 m) is required – as it is gapless and resolves small islands and coastal areas precisely. ArcticDEM often has large elevation errors and significant data gaps close to coastal areas and small islands (e.g. Mankoff et al., 2020). Water Body Mask (WBM) tiles are also supplied with the GLO-90 DEM on the same grid. This provides a convenient way of separating terrestrial and oceanic domains which are consistent with the DEM. We used this product to create a binary land mask by selecting non-ocean pixels.

Using the RGI first order region outlines and the GLO-90 DEM grid shapefile we have selected the required DEM and WBM tiles for each of the investigated RGI regions using the open-source GIS software package QGIS. These tile lists, saved as text files, were used to create DEM and WBM virtual mosaic files in the python geospatial library GDAL. After defining the binary land-ocean masks from the WBM mosaics, we discarded DEM pixels coinciding with the ocean mask to ensure we only retain valid DEM heights for terrestrial areas. The mosaics were then reprojected in GDAL to a 250 m grid referenced in an equal-area projected coordinate system (North Pole Lambert Azimuthal Equal-Area Atlantic; EPSG:3574) to avoid the need for scaling corrections further down the data pipeline due to area distortions (Snyder, 1987; Bamber et al., 2018; Mankoff et al., 2020). Finally, the reprojected DEM and land-ocean mask mosaics were clipped with the RGI region outlines. Henceforth we will refer to these products as COP-250 DEM and COP-250 Land Mask. These products are also used further down the data pipeline as reference grids for snapping.

3.1.2. Ice mask

https://doi.org/10.5194/essd-2024-169
Preprint. Discussion started: 5 August 2024

As the RGI only provides glacier shapefiles for Greenlandic PGICs, we have used two sources for our regional ice masks. Outside of Greenland we used RGI v.6.0 glacier outlines (RGI Consortium, 2017). These are supplied in shapefiles referenced on the WGS-84 ellipsoid. The shapefiles were first reprojected to EPSG:3574 and then rasterised to our reference 250 m grid (i.e. COP-250 DEM grid) using GDAL tools (ogr2ogr, gdal_rasterize). The COP-250 Land Mask was then applied to correct for any potential mismatches (i.e. masking out oceanic pixels) between the RGI and Copernicus datasets.

For the GrIS and Greenlandic PGICs we have used the GIMP v.1 ice mask product (Howat et al., 2014; 2017). This is supplied as a mosaic for Greenland at a 90 m resolution grid referenced in a polar stereographic projection system (NSIDC Sea Ice Polar Stereographic North; EPSG:3413). After reprojecting it in GDAL to the COP-250 DEM grid, which is using the equal area EPSG:3574 projected coordinate system, we applied the COP-250 Land Mask to mask out potential oceanic pixels.

3.2. RCM products

Meltwater runoff and ice albedo both exhibit highly dynamic changes with time, thus we obtained information on these properties from daily RCM outputs provided by MAR v3.11.5 simulations (Fettweis et al., 2013, 2017; Maure et al., 2023) that were forced by hourly ERA5 reanalysis data between 1950 and 2022. This product was chosen as it provides data at relatively high spatial (~ 6 km) and temporal (daily) resolution for a large geographical area, that almost completely covers our region of interest in the Arctic. MAR data cover for 4 separate domains: Canadian Arctic (covering RGI-03 and RGI-04), Greenland (covering RGI-05), Iceland (covering RGI-06), and Russian Arctic (covering RGI-07 and RGI-09). Although the MAR domains only offer partial coverage for the corresponding RGI regions, ice covered areas fall almost completely within the MAR domains, with only a negligible amount of glaciers excluded (Figure 2).

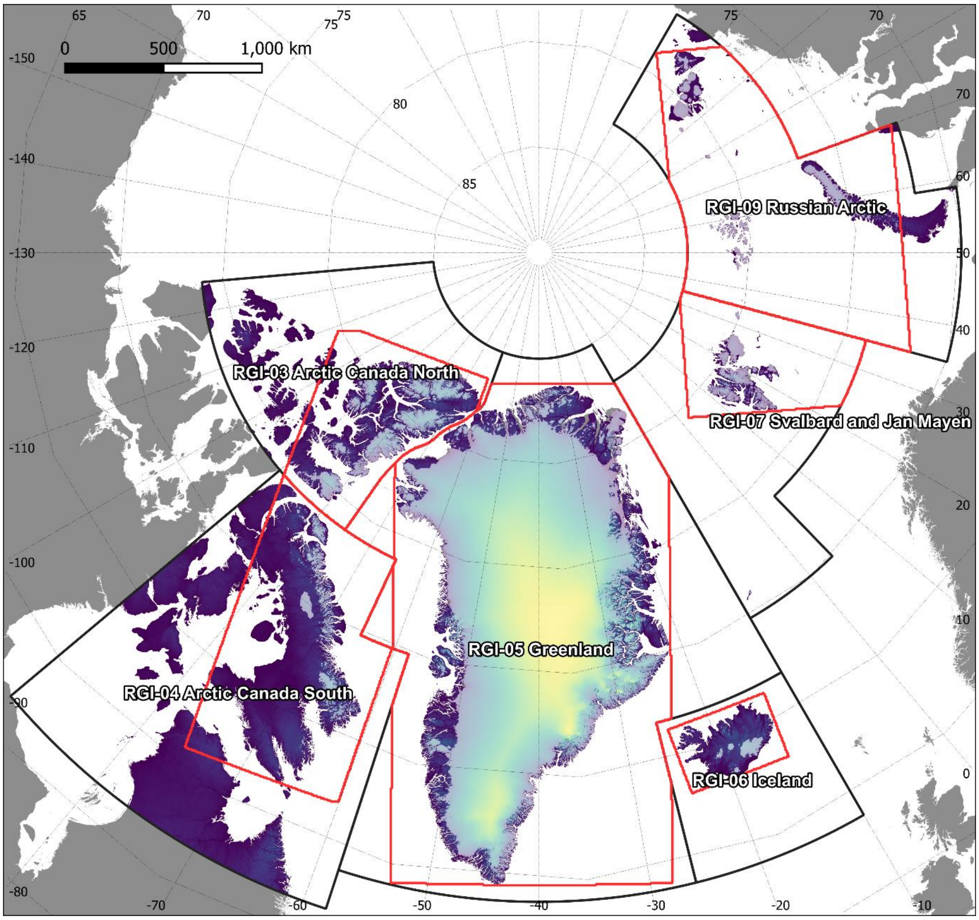

Figure 2. Overview map of our study area showing the COP-250 DEM with the ice coverage overlain (light shading). The investigated principal RGI regions (black line) and the MAR coverage (red line) are both displayed.

MAR products are supplied in netCDF files, with each file holding a year's worth of daily data for a single MAR domain (i.e. there are 72 files for each of the 4 domains). As the files contain many variables, we only extracted those we needed for our calculations (ice runoff, land/tundra runoff, ice albedo, surface elevation, and ice mask) to save computational time. Runoff, R, is defined as

$$R = ME + RA - RT - RF \quad \text{(Eq. 1)}$$

where ME is melt, RA is rainfall, RT is retention, and RF is refreezing.

In lieu of a binary ice mask, this version of MAR introduces fractional ice coverage. Hence, both land runoff and ice runoff data are provided for pixels with partial ice/tundra coverage. The mask also contains generous fringe areas, where ice or tundra coverage is limited (< 0.001

https://doi.org/10.5194/essd-2024-169
Preprint. Discussion started: 5 August 2024

%) and uniform. We simplified these fringe pixels by assuming them to be completely covered by either ice or tundra. The corresponding ice or land runoff values were discarded (i.e. were set to NoData), e.g. a pixel with 0.001% tundra coverage was assumed to be completely covered by ice, thus the corresponding tundra runoff was discarded and ice runoff was assumed to be valid for the whole pixel. This step reduced bias around ice-tundra boundaries, e.g. during reprojection and resampling, and the calculation of vertical gradients.

MAR is referenced in a custom stereographic projection system, with a different set of projection parameters for each domain. In addition, there is a 10° rotation for the Arctic Canada domain, which needs to be reversed before reprojection. All MAR products were reprojected from their custom system to EPSG:3574, while retaining their native 6 km resolution. The reprojected MAR data were then clipped with the appropriate RGI region boundary; this step also brings the MAR domains in line with the RGI regions thereby consolidating our input data. During this step, we also saved the overlapping area between the RGI regions and the MAR domains as shapefiles. This product is used further down the processing pipeline to ensure that we are not extrapolating unreasonably beyond the spatial coverage of valid MAR data. This issue, however, almost exclusively affects land runoff products, as the ice covered regions within the investigated RGI regions are well captured by MAR except for some small islands, e.g. Jan Mayen (Figure 2).

For computational efficiency, we have set up a parallel multiprocessing pool in Python for each of the 6 investigated RGI region, with a dictionary ensuring that the appropriate MAR domain is grabbed during processing. Then, we looped through the 72 years covered by the MAR dataset and submitted each year separately to the pool as an asynchronous task. Altogether 432 tasks were submitted, though the number of active processes and pools were limited due to memory and core number constraints.

https://doi.org/10.5194/essd-2024-169
Preprint. Discussion started: 5 August 2024

4. Methods

4.1. Drainage basins and outflow points

To obtain meltwater discharge volumes at Arctic coastlines, the RCM downscaling procedure needs to be combined with a hydrological routing scheme, which can use either the surface hydraulic head or the subglacial pressure head. In contrast to Mankoff et al. (2020), who assumed meltwater is immediately transported to the bed where it follows the subglacial pressure head, we have opted for a simpler approach and used surface routing exclusively. The principal reason for this is the lack of a pan-Arctic ice thickness product of sufficient accuracy and the relatively large uncertainty in bed topography even over the GrIS. Although, ice thickness estimates are available for all the RGI glaciers (Millan et al., 2022), this dataset is heavily reliant on shallow-ice approximation modelling and only covers Greenlandic PGICs and not the main ice sheet. The BedMachine product, which is based on mass conservation algorithms, is available for the latter region (Morlighem et al., 2017). However, we have sought to avoid relying on multiple datasets based on different methodology for the sake of maintaining data consistency.

The other source of uncertainty inherent to subglacial meltwater routing is due to the complexity of determining the exact timing, location and efficiency of surface-to-bed runoff capture. Although, it is well established that ice surface runoff can penetrate to the bed through ice of arbitrary thickness due to hydrofracturing (Das et al. 2008, Krawczynski et al., 2009), various factor influence this process, e.g. ice surface roughness, the pattern of surface fractures/crevasses, runoff volume, snow/firn thickness and saturation (Igneczi et al., 2018; Davison et al., 2019; Lu et al., 2021). Thus, meltwater can be routed for considerable distances on the ice surface before subglacial capture or proglacial discharge. Accordingly, supraglacial rivers exceeding several dozens of km-s in length, with some terminating at the ice margin, have been observed on the Devon and Barnes Ice Caps and in northern Greenland (Yang et al., 2019; Zhang et al., 2023). Connected to this issue, subglacial pressure head calculations usually assume that subglacial water pressure always equals the ice overburden pressure, i.e. the flotation-factor is constantly 1 (e.g. Mankoff et al., 2020). However, this assumption also introduces uncertainties as it disregards the spatiotemporal evolution of the subglacial drainage system (Davison et al., 2019).

https://doi.org/10.5194/essd-2024-169
Preprint. Discussion started: 5 August 2024

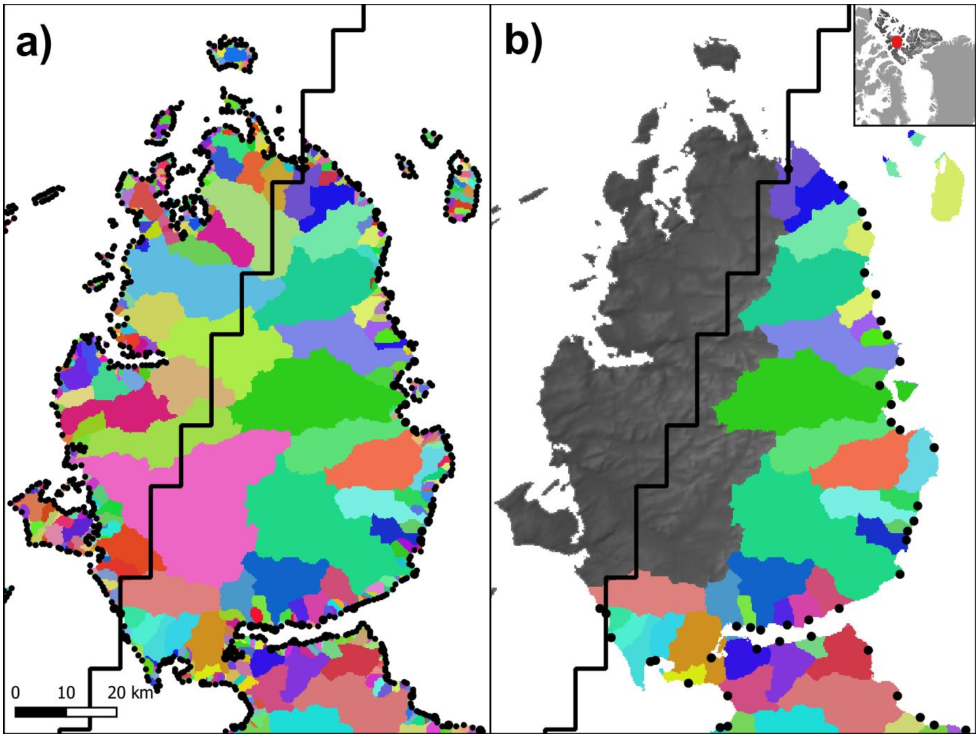

Figure 3. Surface drainage basins and their outflow points (black points) in Northern Canada (a) before and (b) after the removal of small basins and basins that have at least 90% of their area outside the MAR domain (solid black line).

In order to avoid these pitfalls and simplify our approach we used the previously created COP-250 DEM product (Section 3.1.1) to calculate surface drainage basins. These drainage basins were subsequently used to integrate the downscaled daily surface runoff following the approach of Mankoff et al., (2020). The workflow is fully automated by using the Whitebox tools (WBT) package in a Python script. After filling closed depressions and treating flat areas in the COP-250 DEM with the *wbt.fill_depressions* tool (with the fix_flats option checked true), single D8 flow directions were calculated using *wbt.d8_pointer*. Then, distinct drainage basins were derived from the flow directions raster using the *wbt.basins* tool. The resulting product is an integer raster, with unique integers indicating basin coverage (Figure 3). In order to limit the number of basins, thereby aggregating our end product, we removed small basins (< 10 km^2) and set their corresponding pixels to NoData. Then, we allocated these pixels to their nearest valid basin using the *wbt. euclidean_allocation* tool (Figure 3). As this tool also assigns oceanic pixels, we introduced an additional step to mask

https://doi.org/10.5194/essd-2024-169
Preprint. Discussion started: 5 August 2024

out the ocean. We also removed basins that are touching the RGI region outline, buffered with the resolution of the COP-250 DEM. This step ensures that all the drainage basins fall completely within the RGI domain. Data gaps in the RCM products are filled in during the downscaling procedure to facilitate complete spatial coverage (Section 3.3). However, to limit unreasonable spatial extrapolation, we only retained surface drainage basins that have at least 90% of their area within the MAR domain (Figure 3).

Outflow points of the basins were calculated by finding pixels that have no flow direction, i.e. no lower neighbours. These pixels were then converted to vector points and saved to a shapefile. As the COP-250 DEM has previously been treated with the *wbt.fill_depressions* tool with the fix_flat option, these points will represent actual outflow points at the edges of the basins. However, this step also yields the outflow point of basins that have been removed due to their size or coverage (Figure 3). We have sampled the intermediate basin rasters to identify and remove the outflow points that correspond to these removed basins. Thus, the final product has a single outflow point for each valid basin, which is the outflow point associated with the principal basin where fragments from smaller basins are included (Figure 3).

4.2. Vertical gradients of runoff and ice albedo

Localised regression analysis between elevation and modelled climatic parameters has been used in various studies to statistically downscale reanalysis temperatures (e.g.: Gao et al., 2012; 2017; Dutra et al., 2020) and RCM estimates of SMB components (e.g.: Noël et al., 2016). We have adopted a similar approach by utilising inherent localised vertical lapse rates of the daily MAR products (i.e. ice and tundra runoff, ice albedo) and the high resolution COP-250 DEM to statistically downscale MAR from its native resolution of ~6 km to the 250 m resolution COP-250 DEM grid.

First, an 8-neighbourhood moving window was applied to calculate the difference in elevation (i.e. the native DEM in MAR), ice/land runoff, and ice albedo between each pixel and their 8 neighbours. Then, 8D local vertical gradients were determined within the kernel by dividing ice/land runoff, and ice albedo differences with their corresponding elevation differences. NoData was assigned to the centre of the kernel and 0 was assigned to every direction where the elevation difference is below 50 m, the latter step corrects for bias caused by elevation independent runoff and albedo variance.

https://doi.org/10.5194/essd-2024-169
Preprint. Discussion started: 5 August 2024

To yield local vertical gradient rasters, the average of the kernel gradients was assigned to each central pixel if at least 5 valid gradients were found within the kernel. Otherwise, the central pixel was assigned NoData. In lieu of carrying out our own sensitivity analysis, we relied on the conclusions of Noël et al. (2016) who ascertained that using 6 regressions points – i.e. equivalent to 5 valid gradients – provides the best balance between converging to, or diverging from the low resolution RCM runoff products. Positive vertical gradients in ice/land runoff (i.e. runoff increasing with elevation) and negative vertical gradients in ice albedo (i.e. ice albedo decreasing with elevation) were discarded, i.e. assigned NoData. Data gaps were filled in using bilinear interpolation inside the convex hull of valid data, and nearest neighbour extrapolation outside of it.

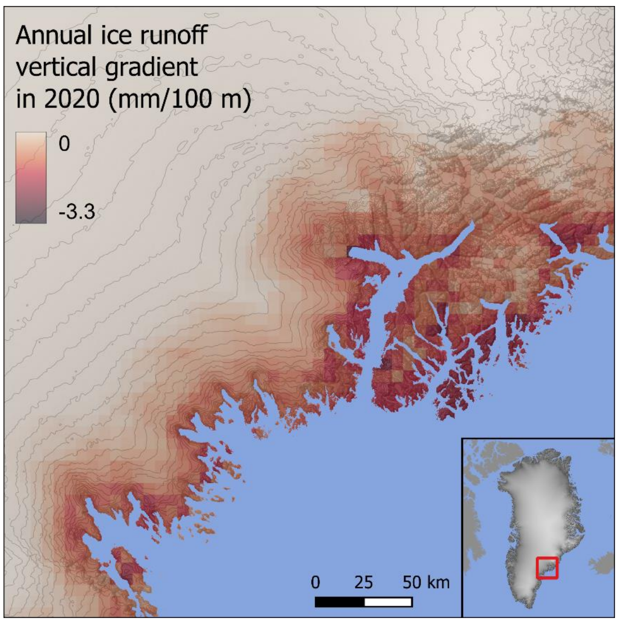

Figure 4. Annual average vertical ice runoff gradient for 2020 in SE Greenland; elevation contours are drawn every 100 m. The annual average is calculated from the daily vertical ice runoff gradients. Units are in mm/100 m, i.e. showing how many mm-s runoff will change with every 100 m elevation gain.

To accurately track the temporal evolution of the vertical gradients, we sequentially looped through each day covered by the MAR products. Thus the process was carried out 26,298 times for each of the 6 RGI domains, producing 473,364 rasters with 6km resolution. Annual time-averaged vertical gradients were also produced and saved to GeoTiffs for reference (Figure 4). To save computational time, the task was integrated with the script that

https://doi.org/10.5194/essd-2024-169
Preprint. Discussion started: 5 August 2024

carries out MAR pre-processing (Section 3.2). This design, in addition to taking advantage of an already existing parallel processing scheme, facilitated efficient I/O operations by writing pre-processed (i.e. filtered, reprojected, clipped) MAR products and their derived localised vertical gradients to the same file – RGI domain specific yearly netCDF files – at the same time.

4.3. Statistically downscaled runoff and ice albedo

The first step of the statistical downscaling algorithm was upsampling the pre-processed MAR ice/tundra runoff, ice albedo (Section 3.2), their vertical gradients (Section 4.2), and the MAR DEM from their native resolution of ~6 km to the 250 m resolution COP-250 DEM grid. Nearest neighbour interpolation was first applied to fill in data gaps, then upsampling to the COP-250 DEM grid was carried out by bilinear interpolation (Figure 5). Once all products were upsampled to the COP-250 DEM grid, elevation differences were calculated between the MAR DEM and the COP-250 DEM (Figure 5). Ice albedo and ice/tundra runoff elevation corrections were then made by multiplying the elevation difference with the appropriate localised vertical gradient raster and adding this to the upsampled ice/tundra runoff and ice albedo rasters (Figure 5). Henceforth we refer to these rasters as the downscaled products. Oceanic pixels were masked out from all of the downscaled rasters by using the high-resolution COP-250 Land Mask; while ice and tundra runoff were masked by the appropriate high-resolution RGI or GIMP ice mask (Figure 5). Pixels with negative runoff were assigned zero.

The downscaling procedure was carried out on the pre-processed daily MAR data, which includes vertical gradients (Section 4.2). Although this procedure was handled separately from MAR preprocessing, the computational setup is similar. A parallel multiprocessing pool was created for each RGI region, then each task running asynchronously on these pools grabbed a single year of data from the appropriate RGI region for processing. Archiving downscaled daily runoff data – which have 250 m spatial resolution – would require excessive storage capacity. To circumvent this problem, we only retained downscaled daily runoff that was summed for the drainage basins. Thus, the algorithm, handling the integration of runoff for the drainage basins (Section 4.4.), was combined with the downscaling procedure. Annual runoff was also obtained for reference by summing the downscaled daily products; these annual rasters were saved to GeoTiffs.

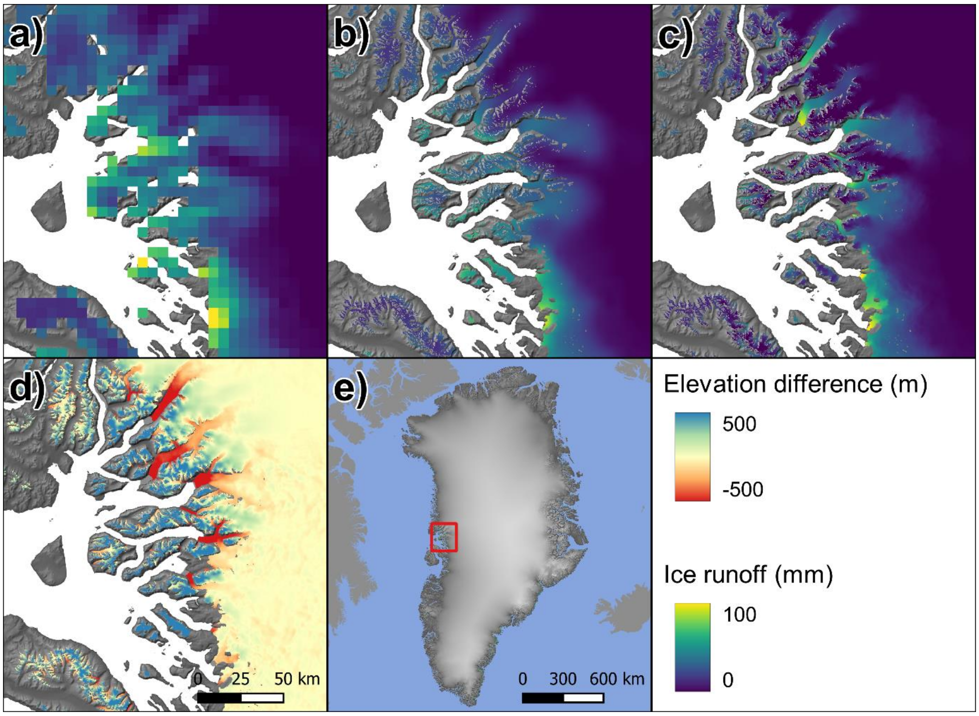

Figure 5. (a) Native resolution daily cumulative ice runoff for 19/July/2022 in W Greenland from MAR; (b) ice runoff after upsampling to 250 m; (c) ice runoff after elevation correction, i.e. downscaling. (d) Difference between the upsampled MAR DEM and the COP-250 DEM. (e) Overview map.

Although our statistical downscaling procedure is similar to the one that was applied on the input data of Mankoff et al. (2020), there are several key methodological differences. Mankoff et al. (2020) used RCM products that have been downscaled to 1 km resolution – following the procedure of Noël et al. (2016) – prior to their data processing, i.e. statistical downscaling was not integrated into their routing algorithm. As the two procedures were separate, the resolution of their routing products (100 m) do not align with the resolution of their downscaled RCM products (1 km), and ice domains do not overlap precisely. To alleviate these spatial discrepancies, Mankoff et al. (2020) scaled and snapped RCM products to the routing resolution. Pixels with mismatching domain types (e.g. land according to RCM but ice according to the routing product) were assigned the average runoff of the corresponding ice/land basin. No runoff was reported for small basins with no RCM coverage of the same type. As we carried out both the downscaling and the routing on the same grid, similar adjustments were not needed in our data processing algorithm.

https://doi.org/10.5194/essd-2024-169
Preprint. Discussion started: 5 August 2024

4.4. Meltwater discharge at outflow points

After downscaling, daily ice and land runoff was summed over each drainage basin. In addition to carrying out this step for whole drainage basins, we also summed ice runoff separately for subsections of the basins where the ice albedo was below 0.7. As this is the minimum allowed albedo for the snow model in MAR (Fettweis et al., 2017), we propose that runoff originating from these regions is a good approximation for runoff from bare ice areas, i.e. below the snow line (BSL). The reason for making this distinction is that, runoff above the snow line will be predominantly due to melt of seasonal snow, while runoff BSL is predominantly ice melt and therefore a reduction in the "ice reservoir". This is an approximation but may be useful for investigating secular versus seasonal fluxes.

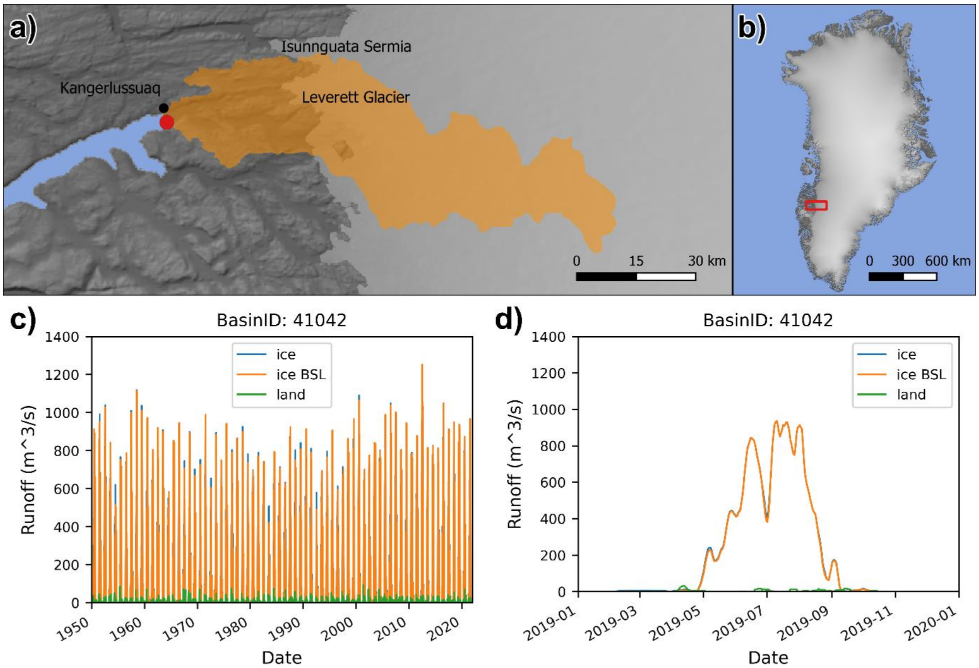

Figure 6. An example of our basin specific daily runoff data. (a) Coverage of the drainage basin, which includes Leverett and Russel Glaciers in West Greenland, and its coastal outflow point, (b) overview map. (c) Seven-day running average of the coastal meltwater discharge from ice, land and bare ice – i.e. ice below snow line (BSL) – runoff between 1950 and 2021, (d) zoomed in view of the same graph between 2019 and 2020.

The resulting basin specific daily runoff time-series were saved into three separate tables – representing land, ice and bare ice runoff (Figure 6) – where rows represent days and columns represent drainage basins. Due to the computational setup (Section 4.3), these

https://doi.org/10.5194/essd-2024-169
Preprint. Discussion started: 5 August 2024

tables were initially saved to yearly RGI domain specific netCDF files. Thus, the final step was concatenating these yearly files, to yield a single netCDF file for each RGI region which contains the daily runoff data for each drainage basin within the region.

4. Product evaluation

To evaluate the performance of our downscaling procedure, we carried out bulk comparisons between our downscaled ice and tundra runoff products and the equivalent datasets from Bamber et al. (2018) and Mankoff et al (2020). While Bamber et al. (2018) provide data for most of the Arctic (but less complete than here), the study of Mankoff et al. (2020) is restricted to Greenland. Thus, two sets of comparisons were performed, one for Greenland and one for the rest of the Arctic. Runoff products computed for the Russian Arctic were excluded from these comparisons, as this region has not been investigated by either of the aforementioned two studies. As our MAR domains – and thus our meltwater discharge dataset – only partially cover some RGI regions, especially in Arctic Canada (Figure 2), and Bamber et al. (2018) provides more complete coverage of the RGI domains, we clipped the Bamber et al. (2018) dataset with our MAR domains (Figure 2). These steps ensured that the compared datasets have similar scope and coverage.

Bulk downscaled ice runoff for Greenland agrees well between the three datasets. Although, the 1σ intervals of the three datasets – when comparing 5-year running means and standard deviations – overlap well (Figure 7a), we estimated slightly larger runoff than the other two datasets. The mean difference between our bulk ice runoff and that of Bamber et al. (2018) and Mankoff et al. (2020) – when comparing datasets before applying running means – is +17.7 Gt and +27.9 Gt, respectively. We propose that the higher resolution of our ice mask and downscaling – 250 m compared to the 1 km and 5 km resolutions of the Mankoff et al. (2020) and Bamber et al. (2018) datasets, respectively – can resolve narrow, low lying glaciers better, which can contribute to higher runoff estimates (Noël et al., 2016). Our estimation for bulk ice runoff from glaciers and ice caps in other Arctic regions outside of Greenland differs to a greater degree from the dataset of Bamber et al. (2018), i.e. with a mean difference of +38.3 Gt (Figure 7c). As glaciers are smaller in these regions – with only a few larger ice caps with flat homogenous plateaus which are easier to resolve in low resolution RCMs – advantages due to the higher resolution of our dataset are even more

https://doi.org/10.5194/essd-2024-169
Preprint. Discussion started: 5 August 2024

pronounced. Some of the difference, however, may also be due to the use of a different re-analysis forcing and a different RCM between the two studies.

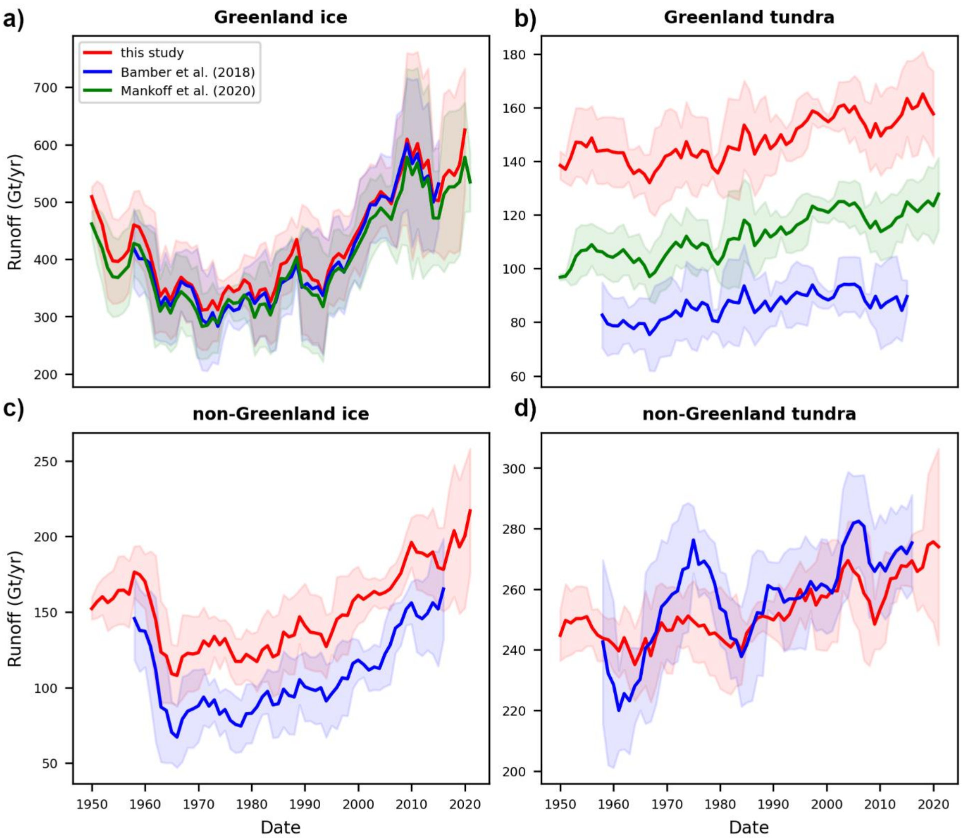

Figure 7. Bulk ice and land/tundra runoff for Greenland and all other Arctic regions, except the Russian Arctic. Graphs show the 5-year running means, while shaded areas show the 5-year running standard deviation. Note that Greenland ice includes PGIC.

Land/tundra runoff estimates from the three datasets for Greenland differ to a larger degree than ice runoff, with the 1σ intervals largely not overlapping (Figure 7b). The mean difference between our bulk land runoff and that of Bamber et al. (2018) and Mankoff et al. (2020) is +61.5 Gt and +36.1 Gt, respectively. These differences can also be explained by the higher resolution of our dataset, which is especially important in Greenland where the region of tundra between the ice sheet and the ocean is narrow, the topography is often rugged, and the coastline is intricate. Bulk runoff increases with the spatial resolution of the datasets (Figure 7a,c), which supports this argument. It is important to note, however, that while the absolute values differ, the trends (and hence freshwater anomalies) are similar. Estimations

https://doi.org/10.5194/essd-2024-169
Preprint. Discussion started: 5 August 2024

for tundra runoff outside of Greenland align better, without a clear pattern of over- or underestimation (Figure 7d). The mean difference between our product and the Bamber et al. (2018) dataset is -5.6 Gt, while the Root Mean Squared Deviation is 16 Gt. This suggests that higher spatial resolution does not offer strong advantages in the estimation of land runoff within this group of RGI regions – including Iceland, Svalbard and Arctic Canada – which is dominated by the vast and relatively flat Canadian Arctic hinterland.

5. Sources of uncertainty

Uncertainties have affected our products at various stages of processing. Firstly, MAR products have introduced a degree of uncertainty into our results due to the physical simplifications of MAR, and the downscaling approach used in conjunction with MAR (e.g. Fettweis, 2020). Although MAR does not provide formal spatiotemporally varying uncertainty products; based on analysis from the Greenland Surface Mass Balance Intercomparison Project (GrSMBIP), its overall uncertainty is approximately ±15% (Fettweis et al., 2020).

The statistical downscaling procedure – which includes corrections applied to the low resolution MAR ice and land masks – has also introduced uncertainty into our runoff products. The degree of this uncertainty cannot be quantified precisely, as we have not carried out a complex evaluation against in-situ runoff observations which are hard to obtain on the field. However, Noël et al. (2016) – who carried out downscaling by applying local gradient driven elevation correction, and going a step further applied an additional albedo correction – demonstrated that statistical downscaling significantly improves local SMB estimations. Their elevation-correction-only downscaling process, which is equivalent to our approach, reduced the RMSE between estimated and observed SMB by 9-23% in the ablation zone (Noël et al., 2016). Hence, at the very least, it is unlikely that our downscaling procedure increased the overall uncertainty of runoff, which already contain MAR uncertainties. The broad alignment of our bulk runoff figures with comparable datasets also reinforces this argument.

The final, coastal meltwater discharge product also has uncertainties due to the simplified hydrological routing procedure. The first of these is caused by the assumption that meltwater is routed on the surface. Meltwater can, and usually does, enter the englacial and subglacial drainage system, where it follows a different hydraulic head. However, it is complicated to quantify the location, timing and magnitude of subglacial capture, and the

https://doi.org/10.5194/essd-2024-169
Preprint. Discussion started: 5 August 2024

exact path this meltwater follows. Therefore, it is difficult to ascertain which approach introduces a larger uncertainty, using surface or subglacial routing exclusively. We have mitigated this uncertainty by providing meltwater discharge only at the coastlines. This implicitly carries out spatial averaging in areas where hydrological routing is only affected by the surface hydraulic head, i.e. the location and magnitude of meltwater discharge at the ice-land interface can be heavily affected by subglacial routing but this effect is weaker downstream. However, this approach cannot mitigate uncertainty in ice-ocean discharge, thus our product is less reliable at these interfaces.

The hydrological routing and the runoff integration procedure, has also assumed that meltwater is instantaneously transported to the discharge point on the coastline. Besides the actual transport time of meltwater within their conduits, which is affected by a complex array of factors, many mechanisms can lead to meltwater retention of various degrees, both in terms of volume fraction and time (Forster et al., 2014). MAR includes an approximation for retention and release of meltwater in the firn layer, and a time delay for bare ice runoff (Fettweis et al., 2013, 2017; Maure et al., 2023), though these are expected to be highly uncertain. Retention, storage, and release of meltwater in the surface- (e.g. in supraglacial ponds, terrestrial lakes and regolith) and subglacial hydrological system (e.g.: in subglacial lakes, cavities, and sediment) are completely unaccounted for. These factors introduce some uncertainty into, the timing and to a lesser degree the volume of meltwater discharge at the coastlines.

6. Code and data availability

Data are available at https://doi.pangaea.de/10.1594/PANGAEA.967544 (Igneczi and Bamber, 2024). Code is available at: https://github.com/ignecziadam/meltwater_discharge.git

Competing interests

The contact author has declared that none of the authors has any competing interests

Acknowledgements

This work was funded by the European Union's Horizon 2020 research and innovation programme through the project Arctic PASSION (grant number: 101003472). We also thank X. Fettweis for providing MAR outputs. JLB was also funded by the German Federal Ministry of Education and Research (BMBF) in the framework of the international future AI lab "AI4EO -- Artificial Intelligence for Earth Observation: Reasoning, Uncertainties, Ethics and Beyond" (grant number: 01DD20001).

https://doi.org/10.5194/essd-2024-169
Preprint. Discussion started: 5 August 2024

References

Bamber, J. L., Tedstone, A. J., King, M. D., Howat I. M., Enderlin, E. M., van den Broeke, M. R., Noël, B.: Land ice freshwater budget of the Arctic and North Atlantic Oceans: 1. Data, Methods, and Results, Journal of Geophysical Research: Oceans, 123, 1827-1837, https://doi.org/10.1002/2017JC013605, 2018.

Biastoch, A., Schwarzkopf, F. U., Getzlaff, K., Rühs, S., Martin, T., Scheinert, M., Schulzki, T., Handmann, P., Hummels, R., Böning, C. W.: Regional imprints of changes in the Atlantic Meridional Overturning Circulation in the eddy-rich ocean model VIKING20X, Ocean Science, 17, 117-1211, https://doi.org/10.5194/os-17-1177-2021, 2021.

Böning, C. W., Behrens, E., Biastoch, A., Getzlaff, K., Bamber J. L.: Emerging impact of Greenland meltwater on deepwater formation in the North Atlantic Ocean, Nature Geoscience, 9, https://doi.org/10.1038/NGEO2740, 2016.

Ciracì, E., Veliconga, I., Swenson, S.: Continuity of the mass loss of the world's glaciers and ice caps from the GRACE and GRACE Follow-on missions, Geophysical Research Letters, 47 (9), https://doi.org/10.1029/2019GL086926, 2020.

Cowton, T. R., Todd, J. A., Benn, D. I.: Sensitivity of tidewater glaciers to submarine melting governed by plume locations, Geophysical Research Letters, 46 (11), 11219-11227, https://doi.org/10.1029/2019GL084215, 2019.

Das, S. B., Joughin, I., Benn, M., Howat, I., King, M., Lizarralde, D., Bhatia, M.P.: Fracture propagation to the base of the Greenland Ice Sheet during supraglacial lake drainage. Science 320, 963–964, https://doi.org/10.1126/science.1153360, 2008.

Davison, B.J., Sole, A.J., Livingstone, S.J., Cowton, T.R., Nienow, P.W.: The influence of hydrology on the dynamics of land-terminating sectors of the Greenland Ice Sheet, Frontiers in Earth Science, 7, https://doi.org/10.3389/feart.2019.00010, 2019.

Delmotte, Zhai, V. P., Pirani, A., Connors, S. L., Péan, C., Berger, S., Caud, N., Chen, Y., Goldfarb, L., Gomis, M. I., Huang, M., Leitzell, K., Lonnoy, E., Matthews, J. B. R., Maycook, T. K., Waterfield, T., Yelekçi, O., Yu, R., Zhou, B. (eds.)]. Cambridge university Press, Cambridge, united Kingdom and New York, NY, USA, https://doi.org/10.1017/9781009157896, 2021.

Dukhovskoy, D. S., Yashayaev, I., Proshutinsky, A., Bamber J. L., Bashmachnikov, I. L., Chassignet, E. P., Lee, C. M., Tedstone, A. J.: Role of Greenland freshwater anomaly in the recent freshening of the Subpolar North Atlantic, Journal of Geophysical Research: Oceans, 124, 3333-3360, https://doi.org/10.1029/2018JC014686, 2019.

Dutra, E., Muñoz-Sabater, J., Boussetta, S. , Komori, T., Hirahara, S., Balsamo, G.: Environmental Lapse Rate for High-Resolution Land Surface Downscaling: An Application to ERA5, Earth and Space Science, 7 (5), https://doi.org/10.1029/2019EA000984, 2020.

Enderlin, E. M., Howat, I. M., Jeong, S., Noh, M. J., van Angelen, J. H., can den Broeke, M. R.: An improved mass budget for the Greenland Ice Sheet, Geophysical Research Letters, 41 (3), 866-872. https://doi.org/10.1002/2013GL059010, 2014.

ESA: Copernicus GLO-90 DEM DGED, https://doi.org/10.5270/ESA-c5d3d65 [Date Accessed: 16/10/2022], 2021.

Fettweis, X., Franco, B., Tedesco, M., van Angelen, J.H., Lenaerts, J.T.M., van den Broeke, M.R., Gallée, H.: Estimating the Greenland ice sheet surface mass balance contribution to

https://doi.org/10.5194/essd-2024-169
Preprint. Discussion started: 5 August 2024

future sea level rise using the regional atmospheric climate model MAR, The Cryosphere, 7, 469-489, https://doi.org/10.5194/tc-7-469-2013, 2013.

Fettweis, X., Box, J.E., Agosta, C., Amory, C., Kittel, C., Lang, C., van As, D., Machguth, H., Gallée, H.: Reconstructions of the 1900-2015 Greenland ice sheet surface mass balance using the regional MAR model, The Cryosphere, 11, 1015-1033, https://doi.org/10.5194/tc-11-1015-2017, 2017.

Fettweis, X., et al..: GrSMBMIP: intercomparison of the modelled 1980–2012 surface mass balance over the Greenland Ice Sheet, The Cryosphere, 14, 3935–3958, https://doi.org/10.5194/tc-14-3935-2020, 2020.

Forster, R. R., Box, J. E., van den Broeke, M., Miège, C., Burgess, E. W., van Angelen, J. H., Lenaerts, J. T. M., Koenig, L. S., Paden, J., Lewis, C., Gogieni, S. P., Leuschen, C., McConnel, J. R.: Extensive liquid meltwater storage in firn within the Greenland ice sheet, Nature Geoscience, 7, 95-98, https://doi.org/10.1038/ngeo2043, 2014.

Frederikse, T., Landerer, F., Caron, L., Adhikari, S., Parkes, D., Humprey, V. W., Dangendorf, S., Hogarth, P., Zanna, L., Cheng, L., Wu, Y. H.: The causes of sea-level rise since 1900, Nature, 584, 393-397, https://doi.org/10.1038/s41586-020-2591-3, 2020.

Gao, L., M. Bernhardt, and K. Schulz, “Elevation correction of ERA-Interim temperature data in complex terrain,” Hydrology and Earth System Sciences, 16(12), 4661–4673, https://doi.org/10.5194/hess-16-4661-2012, 2012.

Gao, L., Bernhardt, M., Schulz, K., Chen, X.: Elevation correction of ERA-Interim temperature data in the Tibetan Plateau, International Journal of Climatology, 37(9), 3540–3552, https://doi.org/10.1002/JOC.4935, 2017.

Gillard, L. C., Hu, X., Myers, P. G., Bamber, J. L.: Meltwater pathways from marine terminating glaciers of the Greenland Ice Sheet, Geophysical Research Letters, 43, 10873-10882, https://doi.org/10.1002/2016GL070969, 2016.

Howat, I.: MEaSUREs Greenland Ice Mapping Project (GIMP) Land Ice and Ocean Classification Mask, Version 1 [GimpIceMask_90m_2015_v1.2]. Boulder, Colorado USA. NASA National Snow and Ice Data Center Distributed Active Archive Center. https://doi.org/10.5067/B8X58MQBFUPA [Date Accessed: 16/10/2022], 2017.

Howat, I.M., A. Negrete, B.E. Smith: The Greenland Ice Mapping Project (GIMP) land classification and surface elevation datasets, The Cryosphere, 8, 1509-1518, doi:10.5194/tc-8-1509-2014, 2014.

Hugonnet, R., McNabb R., Berthier E., Menounos B., Nuth, C., Girod, L., Farinotti, D., Huss, M., Dussaillant, I., Brun, F., Kääb, A.: Accelerated global glacier mass loss in the early twenty-first century, Nature, 592, 726-731, https://doi.org/10.1038/s41586-021-03436-z, 2021.

Igneczi, A., Bamber, J. L.: Pan-Arctic land-ice and tundra meltwater discharge database from 1950 to 2021, PANGAEA, https://doi.org/10.1594/PANGAEA.967544, 2024.

Ignéczi, Á., Sole, A., Livingstone, S., Ng, F., Yang, K.: Greenland Ice Sheet surface topography and drainage structure controlled by the transfer of basal variability, Frontiers in Earth Science, 6(101), https://doi.org/10.3389/feart.2018.00101, 2018.

IPCC: Climate Change 2021: The Physical Science Basis. Contribution of Working Group I to the Sixth Assessment Report of the Intergovernmental Panel on Climate Change [Masson-Delmotte, V., P., Zhai, A., Pirani, S. L., Connors, C., Péan, S., Berger, N., Caud, Y., Chen,

https://doi.org/10.5194/essd-2024-169
Preprint. Discussion started: 5 August 2024

L., Goldfarb, M. I., Gomis, M., Huang, K., Leitzell, E., Lonnoy, J. B. R., Matthews, T. K., Maycock, T., Waterfield, O., Yelekçi, R., Zhou, Y., Zhou, B. (eds.)]. Cambridge University Press, Cambridge, United Kingdom and New York, NY, USA, 2391 pp. doi:10.1017/9781009157896, 2021.

King, M. D., Howat, I. M., Candela, S. G., Noh, M. J., Jeong, S., Noël, B., can den Broeke, M. R., Wouters, B., Negrete, A.: Dynamic ice loss from the Greenland Ice Sheet driven by sustained glacier retreat, Communications Earth & Environment, 1, 1, https://doi.org/10.1038/s43247-020-0001-2, 2020.

Krawczynski, M., Behn, M., Das, S., and Joughin, I.: Constrains on the lake volume required for hydrofracture through ice sheets. Geophys. Res. Lett., 36:L10501. https://doi.org/10.1029/2008GL036765, 2009.

Lu, Y., Yang, K., Lu, X., Li, Y., Gao, S., Mao, W., Li, M.: Response of supraglacial rivers and lakes to ice flow and surface melt on the northeast Greenland ice sheet during the 2017 melt season, Journal of Hydrology, 602, https://doi.org/10.1016/j.jhydrol.2021.126750, 2021.

Mankoff, K. D., Noël, B., Fettweis, X., Ahlstrøm A. P., Colgan, W., Kondo, K., Langley, K., Sugiyama, S., van As, D., Fausto, R. S.: Greenland liquid water discharge from 1958 through 2019, Earth System Science Data, 12, 2811-2841, https://doi.org/10.5194/essd-12-2811-2020, 2020.

Maure, D., Kittel, C., Lambin, C., Delhasse, A., and Fettweis, X.: Spatially heterogeneous effect of the climate warming on the Arctic land ice, Cryosph. Discuss., 2023, 1–20, https://doi.org/10.5194/tc-2023-7, 2023.

Melton, A. M., Alley, R. B., Anandakrishnan, S., Parizek, B. R., Shanin, M. G., Stearns, L. A., LeWinter, A. L., Finnegan D. C.: Meltwater drainage and iceberg calving observed in high-spatiotemporal resolution at Helheim Glacier, Greenland, Journal of Glaciology, 68 (270), 812-828, https://doi.org/10.1017/jog.2021.141, 2022.

Millan, R., Mouginot, J., Rabatel, A., Morlighem, M.: Ice velocity and thickness of the world’s glaciers, Nature Geoscience, 15, 124-129, https://doi.org/10.1038/s41561-021-00885-z, 2022.

Morlighem, M., et al.: BedMachine v3: Complete bed topography and ocean bathymetry mapping of Greenland from multi-beam echo sounding combined with mass conservation, Geophysical Research Letters, 44(21), 11051-11061 https://doi.org/10.1002/2017GL074954, 2017.

Mouginot, J., Rignot, E., Bjørk A. A., van den Broeke, M., Millan, R., Morlighem, M., Noël, B., Scheuchl, B., Wood, M.: Forty-six years of Greenland Ice Sheet mass balance from 1972-2018, Proceedings of the National Academy of Sciences, 116 (19), 9239-9244, https://www.pnas.org/doi/full/10.1073/pnas.1904242116, 2019.

Noël, B., Jan van de Berg, W., Machguth, H., Lhermitte, S., Howat, I., Fettweis, X., van den Broeke, M.R.: A daily, 1km resolution data set of downscaled Greenland ice sheet surface mass balance (1958–2015), The Cryosphere, 10, 2361-2377, https://doi.org/10.5194/tc-10-2361-2016, 2016.

Proshutinsky, A., Dukhovskoy, D., Timmermans, M-L., Krishfield, R., Bamber, J. L.: Arctic circulation regimes, Philosophical Transactions of the Royal Sociate A, 373 (2052), https://doi.org/10.1098/rsta.2014.0160, 2015.

Rantanen, M., Karpechko, A. Y., Lipponen, A., Nordling, K., Hyvärinen, O., Rousteenoja, K., Vihma, T., Laaksonen, A.: The Arctic has warmed nearly four times faster than the globe

https://doi.org/10.5194/essd-2024-169
Preprint. Discussion started: 5 August 2024

since 1979, Communications Earth & Environment, 3, 168, https://doi.org/10.1038/s43247-022-00498-3, 2022.

RGI Consortium: Randolph Glacier Inventory – A dataset of global glacier outlines, Version 6, Boulder, Colorado, USA, NSIDC: National Snow and Ice Data Center, https://doi.org/10.7265/4m1f-gd79 [Date Accessed 17/10/2022], 2017.

Smith, B., Fricker, H. A., Gardner, A. S., Medley, B., Nilsson, J., Paolo, F. S., Holschuh, N., Adusumili, S., Brunt, K., Csatho, B., Harbeck, K., Markus, T., Neumann, T., Siegfried, M. R., Zwally, H. J.: Pervasive ice sheet mass loss reflects competing ocean and atmosphere processes, Science, 368, 1239-1242, https://doi.org/10.1126/science.aaz5845, 2020.

Snyder, J. P.: Map projections–A working manual. Washington, DC: USGPO, 1987.

Tepes, P., Gourmelen, N., Nienow, P., Tsamados, M., Shepherd, A., Weissgerber, F.: Changes in elevation and mass of Arctic glaciers and ice caps, 2010-2017, Remote Sensing of Environment, 261, https://doi.org/10.1016/j.rse.2021.112481, 2021.

Van den Broeke, M. R., Enderlin, E. M., Howat, I. M., Munneke, P. K., Noël, B., van de Berg, W. J., van Meijgaard, E., Wouters, B.: On the recent contribution of the Greenland Ice Sheet to sea level change, The Cryosphere, 10, 1933-1946, https://doi.org/10.5194/tc-10-1933-2016, 2016.

Yang, Q., Dixon, T. H., Myers, P. G., Bonin, J., Chambers, D., van den Broeke, M. R., Ribergaard, M. H., Mortensen, J.: Recent increases in Arctic freshwater flux affects Labrador Sea convection and Atlantic overturning circulation, Nature Communications, 7, https://doi.org/10.1038/ncomms10525, 2016.

Yang, K., Smit, L.C., Sole, A., Livingstone, S.J., Cheng, X., Chen, Z., Li, M.: Supraglacial rivers on the northwest Greenland Ice Sheet, Devon Ice Cap, and Barnes Ice Cap mapped using Sentinel-2 imagery, International Journal of Applied Earth Observation and Geoinformation, 78, 1-13, https://doi.org/10.1016/j.jag.2019.01.008, 2019.

Zhang, W., Yang, K., Smith, L.C., Wang Y., van As, D., Noël, B., Lu, Y., Liu, J.: Pan-Greenland mapping of supraglacial rivers, lakes, and water-filled crevasses in a cool summer (2018) and a warm summer (2019), Remote Sensing of the Environment, 297, https://doi.org/10.1016/j.rse.2023.113781, 2023.